Eddy overturning of the Antarctic Slope Front controls glacial melting in the Eastern Weddell Sea

O. A. Nøst,[1] M. Biuw,[1] V. Tverberg,[1] C. Lydersen,[1] T. Hattermann,[1] Q. Zhou,[1] L. H. Smedsrud,[2] and K. M. Kovacs[1]

Received 15 January 2011; revised 25 May 2011; accepted 23 August 2011; published 12 November 2011.

[1] The Eastern Weddell Sea is characterized by narrow continental shelves and Warm Deep Water (WDW) is located in close proximity to the ice shelves in this region. The exchange of WDW across the Antarctic Slope Front (ASF) determines the rate of basal ice shelf melting. Here, we present a unique data set consisting of 2351 vertical profiles of temperature and salinity collected by southern elephant seals (*Mirounga leonina*) and a profile beneath the Fimbul Ice Shelf (FIS), obtained via drilling through 395 m of ice. This data set reveals variations in salinity and temperature through winter, and using a conceptual model of the coastal salt budget we quantify the main exchange processes. Our data show that modified WDW, with temperatures below −1.5°C, is advected onto the shelf and into the ice shelf cavities by an eddy overturning of the ASF. The onshore Ekman flux of surface waters during summer is the main source of freshwater that leads to the formation of low salinity shelf waters in the region. The modified WDW that reaches beneath the ice shelves is too cold for basal ice shelf melting to create such low salinity water. A high-resolution model of an idealized ASF–continental shelf–ice shelf system supports the conclusions from the data analysis. The inflow of WDW onto the continental shelf and into the ice shelf cavity occurs within a bottom boundary layer where the eddy advection in the model is particularly strong, in close agreement with the observed vertical profile of temperature beneath the FIS.

Citation: Nøst, O. A., M. Biuw, V. Tverberg, C. Lydersen, T. Hattermann, Q. Zhou, L. H. Smedsrud, and K. M. Kovacs (2011), Eddy overturning of the Antarctic Slope Front controls glacial melting in the Eastern Weddell Sea, *J. Geophys. Res.*, *116*, C11014, doi:10.1029/2011JC006965.

1. Introduction

[2] Basal melting of Antarctic ice shelves may have significant impacts on the Antarctic ice sheet and global sea level [*Pollard and DeConto*, 2009], as thinning ice shelves are associated with acceleration of inland ice streams in Antarctica [*Shepherd et al.*, 2002] and Greenland [*Holland et al.*, 2008; *Straneo et al.*, 2010]. Melting ice shelves also provide freshwater to the ocean, which is important for processes such as sea ice and deep water formation [*Beckmann and Goosse*, 2003; *Hellmer*, 2004]. Probably the most important heat source for ice shelf basal melting around Antarctica is the warm Circumpolar Deep Water (CDW), which circulates from the continental slope region, across the continental shelf and into ice shelf cavities at many different locations around Antarctica [*Fahrbach et al.*, 1994; *Walker et al.*, 2007; *Thoma et al.*, 2008; *Nicholls et al.*, 2008a; *Wåhlin et al.*, 2010].

1.1. Ice Shelf–Ocean Interaction in the Eastern Weddell Sea

[3] In the Eastern Weddell Sea (EWS), Warm Deep Water, (WDW), which is derived from the main mass of CDW around 20°–30°E [*Deacon*, 1979], is separated from ice shelves by the Antarctic Slope Front (ASF) [*Gill*, 1973; *Fahrbach et al.*, 1994; *Heywood et al.*, 1998]. In this region the continental shelf is narrow (see Figure 1), and the ice shelves are located in close proximity to the WDW.

[4] Meteorological conditions in the coastal zone of Dronning Maud Land (DML) are dominated by prevailing and stable easterly winds. Fresh, cold surface water is transported onshore within the Ekman layer and dominates the continental shelf, while warmer and more saline WDW is forced downward below the depth of the continental shelf [*Sverdrup*, 1953; *Ohshima et al.*, 1996; *Heywood et al.*, 1998]. This is illustrated by a typical temperature section across the ASF shown in Figure 1. Winds thus reduce the flow of WDW into the ice shelf cavities [*Smedsrud et al.*, 2006]. However, modified WDW does access the cavities despite the effect of the easterly wind [*Smedsrud et al.*, 2006]. Given the potential for melting represented by WDW, direct investigation of both the water masses and dynamic processes on the continental shelf and slope are essential for ocean and climate modeling.

[1]Norwegian Polar Institute, Tromsø, Norway.
[2]Bjerknes Center for Climate Research, Bergen, Norway.

0148-0227/11/2011JC006965

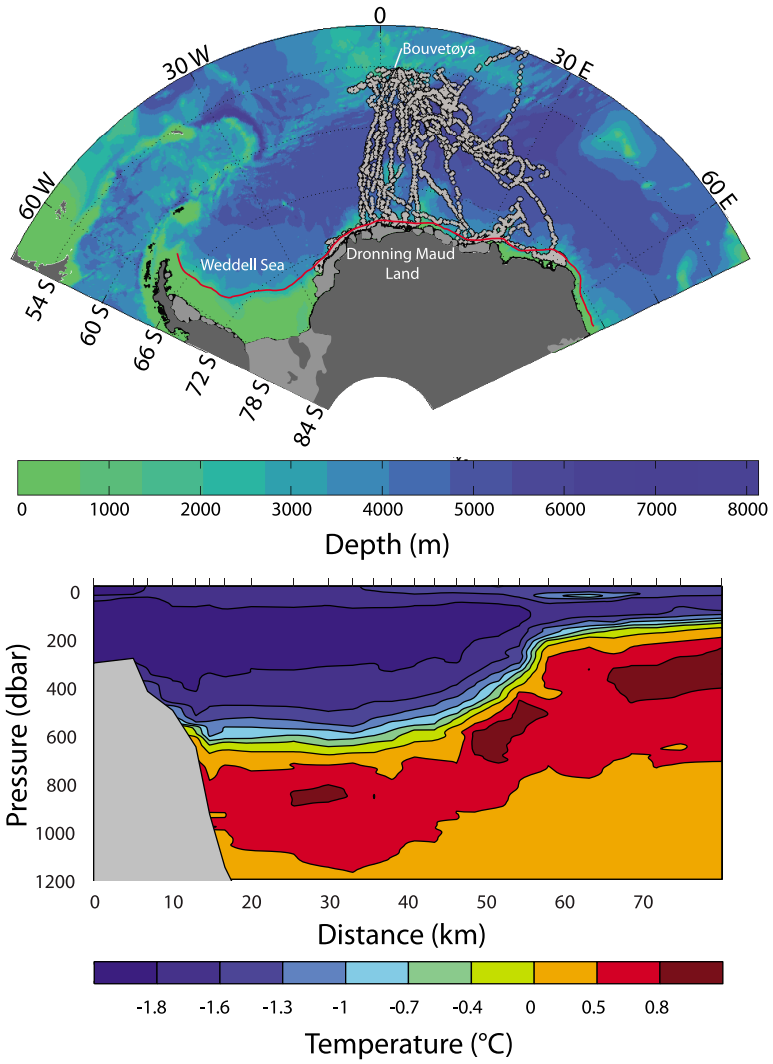

Figure 1. (top) Tracks of seven seals that collected the hydrographic data presented and analyzed in the present paper, shown on top of the Weddell Sea and Southern Ocean bathymetry. Around the Antarctic coast, light gray illustrates the area covered by floating ice shelves and the red line marks the position of the ASF. (bottom) Temperature section across the ASF at 17°W showing the typical structure of the ASF. The section was obtained during the Norwegian Antarctic Research Expedition 1996/1997 [*Nøst and Lothe*, 1997].

[5] Existing estimates of melt water fluxes resulting from basal melting of the EWS ice shelves are mainly based on predictions from ocean models; some of these studies are focused on the Fimbul Ice Shelf (FIS). *Hellmer* [2004] found a FIS melt rate of nearly 5 m/yr, which, despite FIS's relatively small size, was the largest basal mass loss of any of the ice shelves around Antarctica included in his study. In a regional model of the FIS cavity and surrounding ocean, *Smedsrud et al.* [2006] obtained a melt rate of 1.9 m/yr, while *Nicholls et al.* [2008b] obtained an average melt rate of 0.85 m/yr. Even though the latter estimate is significantly lower than the others, *Nicholls et al.* [2008b] argue that it is an overestimate, because their modeled sub–ice shelf temperatures are warmer than real observations measured by an under-ice autosub [*Nicholls et al.*, 2006]. What causes these large variations in modeled melt rates? We suspect that modeled melt rates are crucially dependent on how various models deal with the complex dynamics controlling the overturning of the ASF. Different representations of the ASF in the models could lead to different heat transport into the ice shelf cavities, which again might cause variation in the modeled melt rates.

[6] The ASF is associated with a westward flow of water, the rate of which is in thermal wind balance with the northward density increase [*Heywood et al.*, 1998; *Chavanne et al.*, 2010]. The westward flow therefore decreases with depth, and often reverses direction near the bottom to form the Antarctic Slope Undercurrent [*Heywood et al.*, 1998; *Nunez-Riboni and Fahrbach*, 2009; *Chavanne et al.*, 2010]. Near the bottom along continental slopes, upward-sloping isopycnals are often seen running parallel to the seabed, which again serve to bring WDW closer to the shelf break

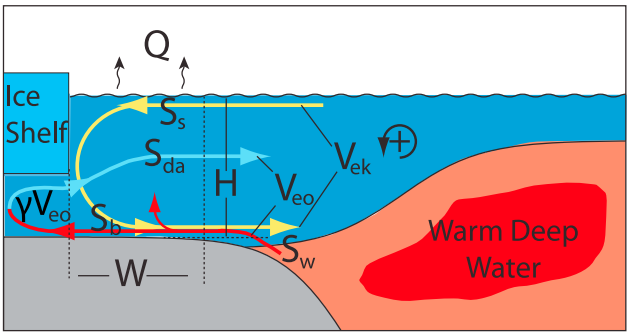

Figure 2. Sketch illustrating the hypothesized exchange processes across the ASF. Yellow arrows illustrate Ekman overturning (V_{ek}), while red and blue arrows illustrate the overturning of the slope front (V_{eo}) and the sub–ice shelf overturning (γV_{eo}) respectively. Other terms are explained in the text.

[*Chavanne et al.*, 2010]. Near bottom upward sloping isopycnals are also clearly seen in the temperature section shown in Figure 1. Today, the dynamical explanation for this phenomenon, which likely plays an important role in the exchange across the ASF, is not clear. However, mechanisms that can explain these phenomenon do exist; one possibility is the interaction of mesoscale eddies with topography.

1.2. Mesoscale Eddies and Frontal Overturning

[7] Mesoscale eddies created by baroclinic instability are a key process behind the overturning circulation in the ocean. The overturning circulation and heat transport across the Antarctic Circumpolar Current (ACC) is largely accomplished by mesoscale eddies (for dynamics of the ACC see the review by *Rintoul et al.* [2001]), and eddies are also essential in structuring the shelf-break front west of Svalbard [*Tverberg and Nøst*, 2009]. Eddies formed by baroclinic instability cause overturning of fronts such that the available potential energy is converted into eddy-kinetic energy; the overturning therefore occurs in the direction that reduces the potential energy. Eddy overturning is often represented as an eddy-induced transport streamfunction [e.g., *Marshall and Radko*, 2003; *Ferrari et al.*, 2010]. In the commonly used parametrization proposed by *Gent and McWilliams* [1990], the eddy-induced streamfunction is given by the local isopycnal slope, which reduces the potential energy everywhere. However, in the eddy parameterizations proposed by *Aiki et al.* [2004] and *Ferrari et al.* [2010], the eddy-induced streamfunction is a non-local function of the properties of the water column. The streamfunction is zero at the surface and at the bottom, and acts as a sink of potential energy for each water column, but not necessarily for each location within the column. This interpretation of eddies opens the possibility that eddies can cause upward sloping isopycnals near the bottom, and locally increase the potential energy, as long as the potential energy is reduced in the water column as a whole. Studies of eddy transports over sloping topography also suggest that eddies can cause upward-sloping isopycnals near the seabed; the main mechanism seems to be mixing of potential vorticity [*Greatbatch and Li*, 2000; *Adcock and Marshall*, 2000]. Thus, eddy transport is a plausible explanation for the upward-sloping isopycnals observed over the continental slope in the EWS [*Chavanne et al.*, 2010].

[8] From the eddy-induced streamfunction and the Eulerian overturning streamfunction, we can construct the residual streamfunction which equals the sum of the other two. The Eulerian streamfunction is obtained by averaging the velocities at constant z-levels. Often, the Eulerian overturning circulation is dominated by wind driven Ekman overturning. It is the residual circulation that describes the movement of a water parcel, and therefore it also describes the advection of a tracer such as heat or salt. The concept of residual circulation was developed in the atmosphere to study the meridional structure by representing eddies as the deviations from a zonal mean (see *Andrews et al.* [1987] for a summary). In the ocean, the concept has been used to understand the overturning circulation of the ACC [e.g., *Marshall and Radko*, 2003]. Here, we will use the concept of residual circulation to explore the overturning circulation of the ASF.

1.3. Working Hypothesis and Outline of the Paper

[9] Our work exploring the exchanges across the ASF is based on the following hypothesis. Assuming that the Eulerian overturning is given by the wind-driven Ekman overturning, and that the eddy-induced overturning is in the direction of reduced potential energy, we create the sketch shown in Figure 2. Because the residual overturning is given by the sum of the oppositely-directed Ekman and eddy-induced overturning circulations, it can flow in either direction. However, as the residual circulation is mainly set by the buoyancy forcing [see, e.g., *Marshall and Radko*, 2003], its direction probably depends on the buoyancy input due to melting of ice shelves and sea ice formation in the area.

[10] We use both hydrographic data and an idealized model to draw conclusions about the details of the exchange processes and overturning circulation of the ASF. In section 2, we present a unique hydrographic data set collected by elephant seals in the coastal zone of DML from 25°W to 50°E through the winter of 2008. We also present a vertical profile of temperature and salinity from beneath the FIS obtained through a hot-water-drilled access hole in December 2009. In section 3, we analyze the data to see whether they are consistent with the hypothesized circulation (Figure 2). In section 4, we present the results from an idealized model of the continental slope shelf–ice shelf system and compare these to the results from the data analysis. In section 5, we discuss the results. Conclusions are listed in section 6. Technical details of the data analysis are given in Appendix A.

2. Observations

2.1. Data Collection and Calibration

[11] All of the hydrographic data, except for the profile from under FIS, were collected by seven southern elephant seals (*Mirounga leonina*) that were captured and equipped with Conductivity-Temperature-Depth Satellite Relay Data Loggers (CTD-SRDLs, developed and built by the Sea Mammal Research Unit, St Andrews, Scotland) on Bouvetøya (54°25′S 3°21′E). These instruments are specially designed for deployment on marine organisms such as seals, whales and turtles. For a detailed description of the instruments see

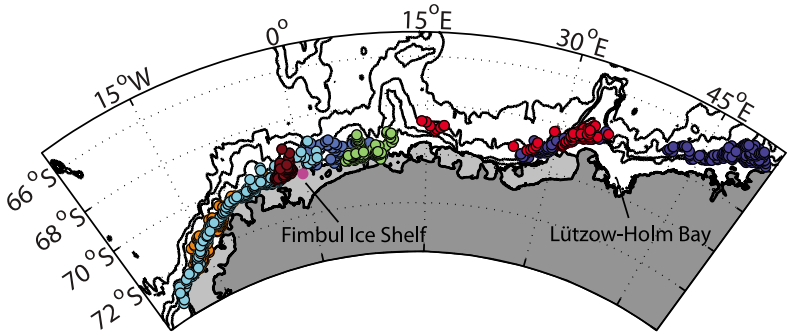

Figure 3. The CTD stations within 100 km from the ice shelf front or coast. Individual seals are represented by different colors. The location of the vertical profile obtained through a hot-water-drilled access hole in the Fimbul Ice Shelf is marked with a magenta point.

Biuw et al. [2007] and *Charrassin et al.* [2008]. The CTD-SRDLs deployed in this study were glued to the heads of the seals using two component industrial epoxy resin according to the methods described by *Fedak et al.* [1983]. Because seals moult annually the instruments fall off approximately 1 year after deployment. Figure 1 shows the tracks of the seals.

[12] The hydrographic data collected by the seals were calibrated against CTD data from the 2008 Polarstern cruise along the zero meridian (E. Fahrbach and G. Rohardt, personal communication, 2008) and against temperature and salinity data from Argo floats [*Gould et al.*, 2004] operating in the area. We used two different methods for calibration. One method compared salinity data at the temperature maximum from the seal tags to data from the Polarstern cruise. The second method compared salinity data from the seal tags to Polarstern and Argo data interpolated on potential temperature surfaces [*Owens and Wong*, 2009]. The two methods lead to constant (in time) salinity offsets that were in good agreement; the data were corrected with offsets between 0 and 0.1 psu. Temperature was calibrated by comparing observed minimum temperatures near the coast to the freezing point temperatures [*Jackett et al.*, 2006] and corrected by constant (in time) offsets between 0.03 and 0.05°C. Accuracies are estimated to be better than 0.03 psu for salinity and 0.02°C for temperature.

[13] Temperature and salinity profiles from beneath the FIS were collected through a hot-water-drilled access hole at 70°18.8′S and 0°6.1′W (Figure 3) in December 2009. The hole was drilled through 395 m of ice where the water depth to the seabed was 876 m. We used an SBE 49 Fastcat CTD sensor with a Power and Data Interface Module (PDIM) and an SBE 36 Deck Unit to take measurements.

2.2. A Coastal Hydrographic Data Set

[14] Our data analysis goal is to test whether temporal variations in temperature and salinity of the shelf water masses is in agreement with the hypothesized exchange processes (Figure 2). To do this we need a temperature and salinity data set representing the shelf water masses, which we will now construct from the hydrographic data collected by the seals. This data set consists of 2351 vertical salinity and temperature profiles located within 100 km of the Antarctic coast/ice front between 25°W and 50°E, during the period from 4 February to 31 October 2008 (Figure 3). In this region the water masses are often close to homogeneous on the shelf, while a sharp thermocline separates the cold and fresh shelf water masses from the WDW that lies over deeper waters. Because the thermocline in the region is very pronounced, its depth can be estimated well by simply finding the depth were the temperature reaches a value that is $\Delta T = 0.3°C$ higher than the surface temperature. For profiles having a thermocline according to this definition, the water masses below the thermocline are removed. Of the 2351 CTD profiles, 1336 were nearly homogeneous and did not have a thermocline, and they are all included in the coastal data set. The profiles without a thermocline are located on the shelf close to the ice front/coast (about 70 % of these profiles were within 10 km of the ice front).

[15] After removing data from below the thermocline we divide the data into pressure bins: 0–10 dbar, 10–20 dbar, 20–50 dbar, 50–100 dbar, and beyond at 50 dbar intervals down to 500 dbar. Furthermore, we apply a time-binning with a bin size of 30 days around each reference day. The pressure- and time-bins make up a grid. Figure 4 shows the number of observations within each bin and the standard deviations of temperature and salinity. All bins with less than 10 observations are excluded, but this has little effect because the number of observations within each bin is usually a lot more than this (Figure 4). The coastal hydrographic data set illustrated by Figure 4 gives good coverage of the coastal zone during the entire winter.

2.3. Results

[16] The temperature and salinity of all of the data points in the coastal data set (after removal of the water below the thermocline, but before binning) are shown in Figure 5. We clearly see how the water column becomes increasingly homogeneous with time and that the minimum salinity increases. The salinity increases observed in the far east (seal no. 1) and far west (seal no. 5, seal locations are shown in Figure 3) are quite similar. This indicates that the salinity increase occurs all along the coast. The maximum salinity varies between 34.3 and 34.4 psu with a minimum reached around July. The minimum temperature equals the surface freezing point except for the observations by seals number 3, 5 and 7 that reported temperatures below −2°C, which indicates interaction with the base of ice shelves. After April

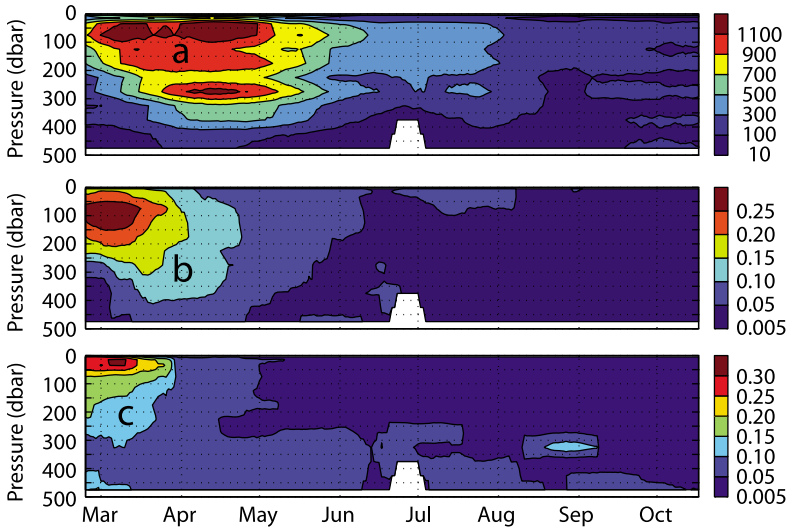

Figure 4. (a) Numbers of observations, (b) standard deviation in salinity (in psu) and (c) standard deviation in temperature (in °C) within each time-pressure bin.

the maximum temperatures are about −1.6°C. This value is of course influenced by the method used, which removed the part of the profile beneath the thermocline. But the data set also includes 1336 profiles without thermoclines that are mainly located on the shelf, and these profiles indicate that waters warmer than −1.6°C are not found on the shelf.

[17] Because water mass characteristics seem to be fairly similar along the coast, the binned data set (Figure 6) probably shows realistic temporal variation that occurs all along the coast. Because the time-bins are 30 days wide (centered on each day), the salinity and temperature fields should be viewed as running means within a 30-day time window. In February and March the surface waters are fresh and warm. Into the fall the water gradually cools while the fresh surface layer deepens, and gradually gets more saline. In late winter, the water column is close to homogeneous in salinity. The temperature of the water column is nearly homogeneous from the beginning of April, except for slightly warmer water found near the bottom.

[18] The observed variability in salinity and temperature are controlled by exchange processes across the ASF. To extract information about these processes, we will use our

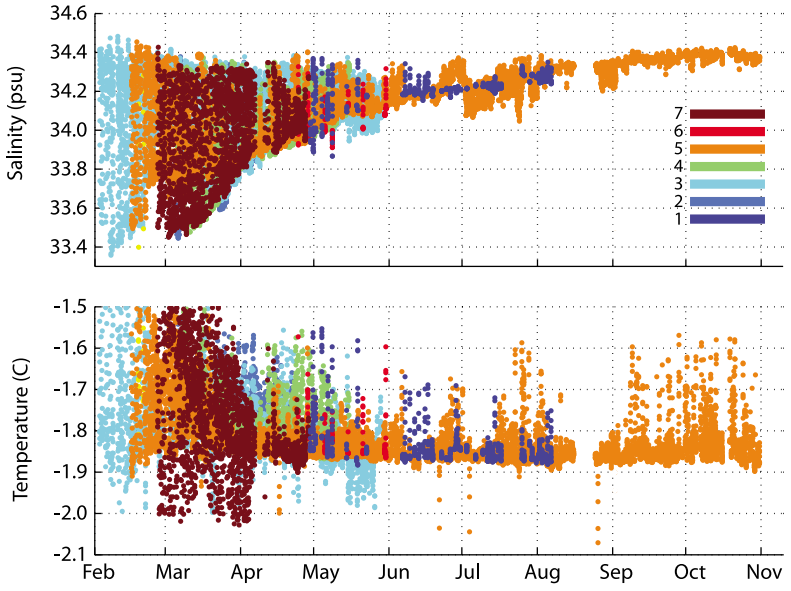

Figure 5. Salinity and temperatures from each data point within 100 km of the ice front/coast and above the thermocline plotted against time. The individual seals are represented with the same colors as in Figure 3.

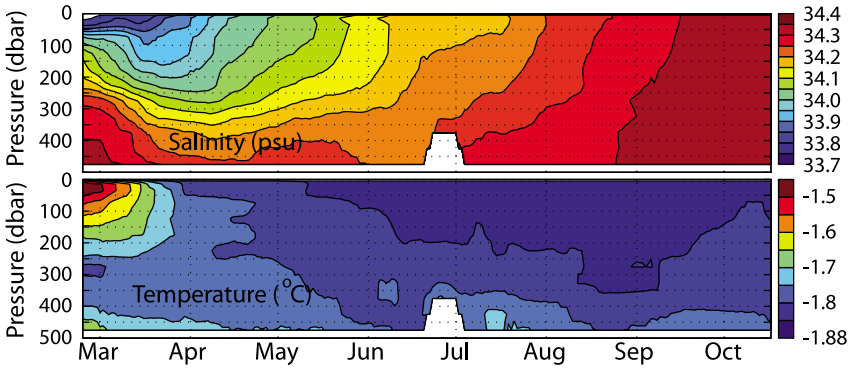

Figure 6. Salinity and temperature within each pressure bin plotted against time. Each bin includes data from 15 days before and after, which works similar to a running mean with a 30 days time window.

observations in a simple conceptual model that describes the coastal salinity budget.

3. A Conceptual Model of the Coastal Salinity Budget

[19] In this section we attempt to reconstruct the coastal salinity budget using real data, revealing the most important exchange processes that transport heat into close proximity with the ice shelves. Due to the importance of melting and freezing processes, the salt and heat budgets are closely connected. However, constructing a model that simultaneously treats both the salt and heat budgets also leads to high noise levels. Therefore, we find it most useful to explore the salinity budget in detail, while the heat budget is only analyzed crudely in the discussion.

3.1. Main Assumptions and Simplifications

[20] We will now construct a conceptual model of the salinity variations of the shelf waters. We assume that the main exchange processes are the ones illustrated in Figure 2; these are eddy and Ekman overturning circulations, the input of freshwater by sub–ice shelf melting and the effect of brine release by sea ice formation. We consider the volume of water over the continental shelf, which is given by the width (W) and depth (H) of the shelf. Eddy overturning of the ASF (V_{eo}) brings relatively saline (and warm) modified WDW onto the shelf near the bottom while less saline water exits higher in the water column. Some of the modified WDW flows into the ice shelf cavity as part of the sub–ice shelf overturning where it is cooled and freshened by interactions with the ice-shelf base. This combined eddy overturning of the ASF and sub–ice shelf overturning is illustrated with the red and blue arrows in Figure 2. Ekman fluxes also play an important role because the prevailing easterly winds transport fresh surface waters into the volume, while the observed westward ocean currents in the region [*Fahrbach et al.*, 1992; *Heywood et al.*, 1998; *Chavanne et al.*, 2010] creates bottom Ekman layers that transport bottom water out of the volume. The overturning circulation resulting from the surface and bottom Ekman fluxes are shown by the yellow arrows (Figure 2). The eddy and Ekman overturning are thought to be responsible for the main exchange of water masses between the continental shelf and slope. However, coastal polynyas lead to large heat losses to the atmosphere which again lead to sea ice formation, with concomitant brine release. This will have an impact on the salinity budget; the effect of this is represented in the model.

[21] Our salt budget model ignores precipitation and also possible melting due to the summer heat, which is seen in the relatively warm temperatures in March (Figure 6). Both of these factors can have an effect in February/March, but are most likely negligible from the beginning of April through the winter. In winter, precipitation will fall mostly on sea ice because the ice cover is extensive (>80 percent in April and ~90 percent from May to November) as seen from the AMSR-E sea ice concentrations. However, even the precipitation that falls on sea water in the leads during winter is not likely to cause freshening of the water column because this water freezes and sea ice is produced in the leads. Therefore, precipitation will influence the salt budget only in summer when temperatures are above freezing (Figure 6). The same seems to be the case for melting driven by heat stored in the water column. The model accounts for the melting driven by modified WDW flowing into the ice shelf cavities, which is the main heat source in winter when the water column has temperatures close to the surface freezing point. In February and March the water column contains heat that might lead to basal ice shelf melting. For simplicity, we have chosen to ignore this heat, but we keep in mind that the freshwater input in February and March may be underestimated in the salinity budget described by the model.

3.2. Deriving the Salinity Budget Terms

[22] The rate of change of salinity caused by the eddy overturning within the volume described by H and W (see Figure 2) is given by

$$WH\left(\frac{dS_{da}}{dt}\right)_{eo} = V_{eo}(S_{da} - S_w) - \gamma V_{eo}(S_{is} - S_w), \qquad (1)$$

where V_{eo} is the transport of the eddy overturning, S_{da} is the depth averaged salinity, S_w is the salinity of the modified WDW advected onto the shelf and S_{is} is the salinity of the water that is flowing out of the ice shelf cavity. γ is a parameter between 0 and 1 determining the relative fraction of the transport V_{eo} that brings water in contact with the base of the ice shelf. Thus, we assume that the sub–ice shelf overturning transport equals $-\gamma V_{eo}$ (see Figure 2). The

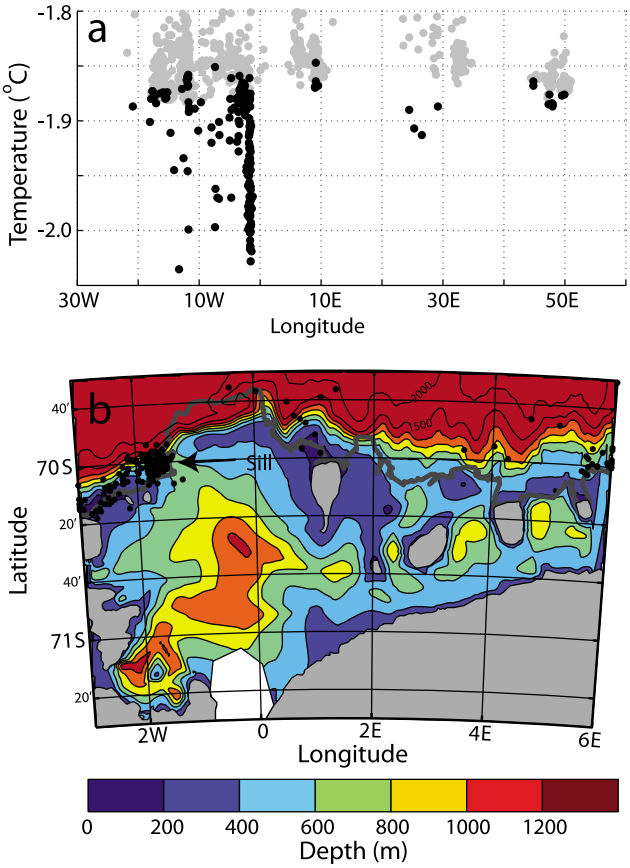

Figure 7. (a) The minimum temperature of each profile plotted against longitude. Gray dots mark temperatures above the freezing point for surface pressure, while black dots mark temperatures below the freezing point. (b) A map of the seabed beneath the FIS [*Nøst*, 2004] with black dots indicating the locations of hydrographic profiles. The solid line marks the FIS ice front. The coldest water is observed near the sill connecting the FIS cavity with the surrounding ocean.

representation of eddies, using the eddy transport V_{eo}, is in agreement with the usual method of representing eddies with an eddy-induced transport streamfunction [*Marshall and Radko*, 2003; *Ferrari et al.*, 2010]. We have chosen to use the depth-averaged salinity as the salinity of the water flowing out of the volume due to the eddy overturning. This is because the density gradients associated with the ASF are most pronounced at depth, and therefore we assume that the eddy overturning cell does not reach the surface. The depth-averaged salinity is therefore thought to represent the outflowing water better than the surface salinity.

[23] The next step is to find a value for the salinity S_{is}. We assume that the source water in the interaction with the ice shelves is modified WDW, with salinity S_w and temperature T_w, that is upwelled onto the continental shelf by the eddy overturning (S_w and T_w will be determined by water mass analysis in the next section). We assume that the water flowing out of the ice shelf cavities upwells to the surface and reaches the surface freezing point, T_f. We believe this is a good assumption because we only observe water that is significantly colder than T_f at one 50-km wide location (see Figure 7) along 3000 km of coastline, while the rest of the coastline is dominated by water masses with temperatures near the freezing point. We can now find its salinity, S_{is}, from the melting/freezing T-S relation, also called the "Gade line" [*Gade*, 1979; *Nøst and Foldvik*, 1994]:

$$S_{is} = S_w\left(1 - \frac{c}{L}\left(T_w - T_f\right)\right). \tag{2}$$

Here, c is the specific heat capacity for sea water and L is the latent heat of fusion. Combining this with equation (1) gives

$$WH\left(\frac{dS_{da}}{dt}\right)_{eo} = V_{eo}(S_{da} - S_m), \tag{3}$$

where S_m is given by

$$S_m = S_w\left(1 - \gamma\frac{c}{L}\left(T_w - T_f\right)\right). \tag{4}$$

Equations (3) and (4) express salinity changes due to eddy overturning of the ASF.

[24] In deriving the term representing salinity change due to Ekman fluxes, we assume that the westward geostrophic currents are mainly wind-driven in such a way that the bottom Ekman flux generally equals the surface Ekman flux along the coast. In the Nordic Seas and Arctic Ocean, we see that bottom Ekman transports and surface Ekman transports balance each other over the scale of ocean basins [*Nøst and Isachsen*, 2003]. We therefore believe it reasonable to assume that the bottom Ekman transport is, on average along the coast, equal and opposite to the surface Ekman transport. The rate of change of salinity as a result of the Ekman overturning is then

$$WH\left(\frac{dS_{da}}{dt}\right)_{ek} = V_{ek}(S_s - S_b), \tag{5}$$

where V_{ek} is the Ekman transport, S_s is the surface salinity and S_b is the bottom salinity. Although eddy overturning and Ekman overturning both involve flow at the bottom, we use S_b as the salinity being advected by the Ekman transport and S_w as the salinity advected by the eddies. The reason for this is that the two overturning circulations have different directions. Eddy overturning transports modified WDW onto the shelf, while the Ekman overturning transports the densest shelf waters off the shelf. Thus, the eddy overturning is advecting the salinity S_w, while the Ekman overturning is advecting the along-shore-averaged bottom density S_b.

[25] The rate of change of salinity driven by a sea ice formation rate, I, is given by

$$WH\left(\frac{dS_{da}}{dt}\right)_{if} = IW(S_{da} - S_i), \tag{6}$$

where S_i is the salinity in the newly formed ice [*Smedsrud and Skogseth*, 2006; *Notz and Worster*, 2008]. Q represents the heat loss to the atmosphere per area and α is a parameter between 0 and 1 that determines the relative allocation of heat loss towards ice formation (α = 1) or to

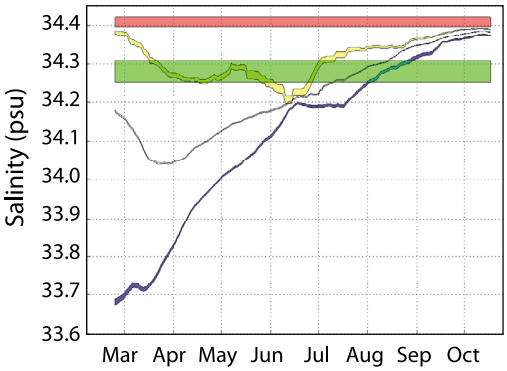

Figure 8. The surface salinity (S_s, blue), the depth averaged salinity (S_{da}, gray), the bottom salinity (S_b, yellow), the source water salinity (S_w, red) and the lowest possible salinity resulting from interaction with the ice-shelf base (S_{is} or S_m with $\gamma = 1$, green).

cooling of the water masses ($\alpha = 0$). Sea ice formation can then be derived from the heat flux αQ to give

$$WH\left(\frac{dS_{da}}{dt}\right)_{if} = \alpha\frac{QW}{\rho L}(S_{da} - S_i). \quad (7)$$

[26] Combining eddy overturning (equation (3)), Ekman overturning (equation (5)) and the brine release due to sea ice formation (equation (7)) gives the total salinity budget:

$$WH\frac{dS_{da}}{dt} = V_{ek}(S_s - S_b) + V_{eo}(S_{da} - S_m) + \alpha\frac{WQ}{\rho L}(S_{da} - S_i). \quad (8)$$

The next step is to estimate the different terms from the data with the goal of identifying the main exchange processes.

3.3. Estimating the Salinity Budget From Data

[27] Salinity and temperature as functions of pressure and time are shown in Figure 6. We calculate S_{da}, S_s, S_b and dS_{da}/dt using these data. The details regarding our estimation of these variables and their uncertainties are given in Appendix A1. The results are shown in Figure 8.

[28] V_{eo} represents the advective transport due to eddies, which transport modified WDW with salinity S_w onto the continental shelf and into the ice shelf cavities. S_w is estimated by water mass analysis using a T-S plot of all the individual data points from the seals (not averaged within bins) and the data from beneath the FIS (Figure 9). The water with temperatures colder than the surface freezing point (Ice Shelf Water, ISW) are observations from the specific location where ISW is observed (see Figure 7) and from the profile from beneath the FIS. Since S_w and T_w characterize the source of the water masses found beneath the ice shelf they should be located on the melting/freezing line [*Gade*, 1979; *Nøst and Foldvik*, 1994] going through the salinity and temperatures of the sub–ice shelf water masses. Additionally, the ISW observed outside the FIS appears to have very stable characteristics, since the seal data collected in 2008, the measurements made under the FIS collected in 2010 and observations obtained during 2005 [*Nicholls et al.*, 2006; *Price et al.*, 2008] all show similar characteristics. Therefore, we believe the source water is also stable and is present year-round. Under these conditions, the most likely source water is found where the melting/freezing line intersects the line illustrating mixing with WDW (red line in Figure 9), as this water mass is present all year. The conclusion from this is that the modified WDW transported onto the shelf by V_{eo} originates in the thermocline separating the cold shelf waters from the WDW. The estimates of S_w and T_w are shown in Figure 9, and S_w and S_m are both shown in Figure 8.

[29] Sea ice formation depends on atmospheric parameters as well as sea ice concentration, while the Ekman transport, V_{ek}, is determined from the along-shore component of the stress acting on the ocean surface. This stress depends on atmospheric parameters as well as sea ice concentration and dynamics. To estimate sea ice formation and Ekman transport we use atmospheric data from NCEP [*Kalnay et al.*, 1996] and AMSR-E sea ice concentration data [*Spreen et al.*, 2008] together with surface hydrography from the seal-borne instruments. The details are given in Appendix A2 and A3, where we also discuss uncertainties.

[30] W and H are crucial parameters for the model. We estimate both from the ETOPO1 data set [*Amante and Eakins*, 2008]. W is set equal to the average distance between the ice front (or the coast where there are no ice shelves) and the 500 m isobath. Negative distances (where the ice front overhangs water deeper than 500 m) is set to zero before averaging. We find $W = (12 \pm \delta_W)$ km and $H = (400 \pm \delta_H)$. The uncertainties δ_W and δ_H are difficult to estimate. But we set $\delta_W = 2$ km and $\delta_H = 50$ m.

[31] We can now estimate all of the terms in equation (8). We do this by solving for the eddy overturning term, $V_{eo}(S_{da} - S_m)$, because all of the other terms are directly determined from the data. The magnitudes of the different terms and their uncertainties are shown in Figure 10. Details

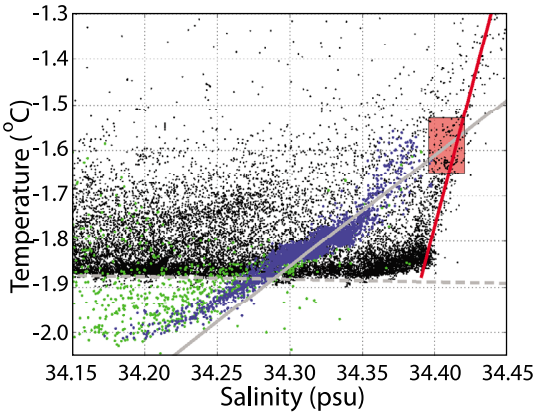

Figure 9. T-S diagram including all seal data (profiles with temperatures below the freezing point for surface pressure are shown in green, while the rest of the seal data are shown in black) and the profile from beneath the FIS (blue). The dashed gray line marks the freezing point for surface pressure, the gray solid line shows the melting/freezing TS relation [*Gade*, 1979; *Nøst and Foldvik*, 1994] and the red line illustrates mixing with WDW. The red square marks the estimated temperature and salinity for the source water of the observed ISW.

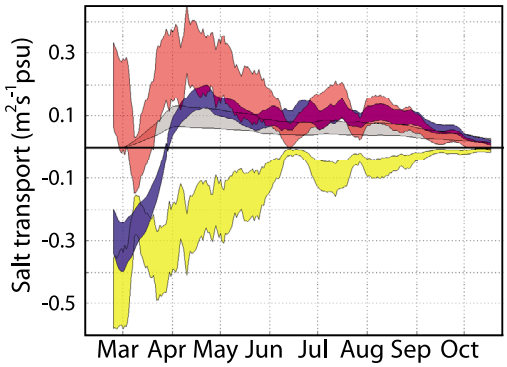

Figure 10. The different terms in the salinity budget (equation (8)). The change of salt content with time ($WH\frac{dS_{da}}{dt}$) is shown in blue, Ekman overturning ($V_{ek}(S_s - S_b)$) is shown in yellow, the sea ice formation ($\alpha\frac{WQ}{\rho L}(S_{da} - S_i)$) is shown in gray and eddy overturning ($V_{eo}(S_{da} - S_m)$) is shown in red.

regarding uncertainty estimation are given in Appendix A4. The resulting picture is largely consistent with the circulation illustration depicted in Figure 2. The Ekman overturning has a freshening effect on the salinity consistent with a positive V_{ek}. After April, ice formation causes a salinification that is close to the observed rate of change of salinity. However, for the salinity budget to balance, the transport due to V_{eo} must increase the salinity (except in March, where V_{eo} is shown to decrease the salinity, which is probably a result of the underestimate of freshwater input during February and March as discussed above). Before August, this is consistent with a negative V_{eo} (as in Figure 2) as S_m is larger than S_{da} (Figure 8), but from August to October V_{eo} can be positive or negative depending on the amount of interaction with the ice shelves. For $\gamma = 1$, $S_{da} - S_m$ changes sign in August and remains negative through into the autumn (Figure 8). In order to keep increasing the salinity, V_{eo} also has to change sign so that $V_{eo}(S_{da} - S_m)$ is always positive. However, as V_{eo} is a transport representing eddy overturning of the front it should act to reduce potential energy, and V_{eo} can therefore not be positive. Thus, $S_{da} - S_m$ must be less than zero in order for our salinity budget to be dynamically consistent, and for $\gamma = 0$ this is always true. It can be argued that it would be more correct to use the surface salinity S_s as the outflow due to the fact that eddy overturning will take place near the surface or at least in the upper part of the water column. As $S_s < S_{da}$, this would lead to greater dynamical consistency. However, the difference between S_{da} and S_s is not very large in winter (Figure 8), and for the salinity budget to be consistent with the hypothesized dynamics (Figure 2), some of the source water must mix with the coastal water without first interacting with the ice shelf, which is equivalent to setting $\gamma < 1$. We think that this is quite realistic because water coming onto the shelf does not necessarily have to flow into the ice shelf cavity. Therefore, we conclude that the observed variability in salinity is largely consistent with the circulation patterns illustrated in Figure 2. However, we would like to see more evidence that the exchanges across the ASF are really consistent with Figure 2, and the next step is therefore to set up a numerical ice shelf–ocean model of the ASF circulation and exchange.

4. Modeling

[32] The circulation shown in Figure 2 consists of two oppositely-directed overturning circulations; the Ekman overturning and the eddy overturning. Our analysis of the data suggests that Ekman overturning is the main process causing freshening of the coastal water masses, while the eddy overturning is vital in bringing heat towards the ice shelves. To look more closely at this description of the circulation we have set up an idealized model of the ASF–continental shelf–ice shelf system.

4.1. Setup

[33] For the idealized modeling, we have used the Regional Ocean Modeling System (ROMS) [*Shchepetkin and McWilliams*, 2005; *Dinniman et al.*, 2007] set up in a channel with periodic boundary conditions in the along-slope direction. The domain is 480 by 300 km and topography varies in a cross-channel direction (300 km) as shown in Figure 11a. The horizontal grid resolution is 1.5 km with 30 vertical layers. The topography of the model has similarities to the FIS cavity, including water depths ranging from 400 m at the northern sill to 800 m at the southern boundary. The model is initialized with temperature and salinity fields that were constructed from a cross-slope CTD section at 17°W (Figure 1) by removing fresh and warm surface waters, making it more similar to winter hydrography. Beneath the ice shelf, the model is initialized with vertical, linear sub–ice shelf profiles of temperature and salinity resembling our observations beneath the FIS. The initial temperature field is shown in Figure 11a. To minimize the pressure gradient force error, typical of S-coordinate models, the abrupt ice edge is replaced by a smoother transition to open water. This will have an effect on the exchange as the topographic step of the ice front represents a potential vorticity barrier. However, a perfect representation of the ice front is not possible due to pressure gradient effects, so the ice front will be quite smooth in any case. Test runs with more realistic ice fronts show no qualitative differences in distribution of water masses and circulation beneath the ice shelf. Since we are more interested in the structure of the inflowing modified WDW than the actual rate of exchange, we chose to use the smooth ice front.

[34] For computational efficiency, the maximum water depth was limited to 2000 m, although the bathymetry north of the coast of DML exceeds 5000 m. Further technical details about the model runs can be summarized as follows: (1) vertical grid resolution is enhanced close to the surface and near the seabed; (2) the layer thicknesses vary from 2.5 m in the surface layer up to 125 m in the deep ocean interior; (3) vertical grid resolution through the ASF never exceeds 40 m; (4) quadratic bottom friction drag is applied at the seabed as well as below the ice shelf and free slip conditions are applied along the vertical boundaries; (5) thermodynamics and pressure at the ice shelf base follows *Dinniman et al.* [2007]; (6) horizontal advection of tracers (potential temperature and salinity) and momentum are achieved by an upwardly biased third-order advection scheme; while a fourth-order centered scheme was used for vertical advec-

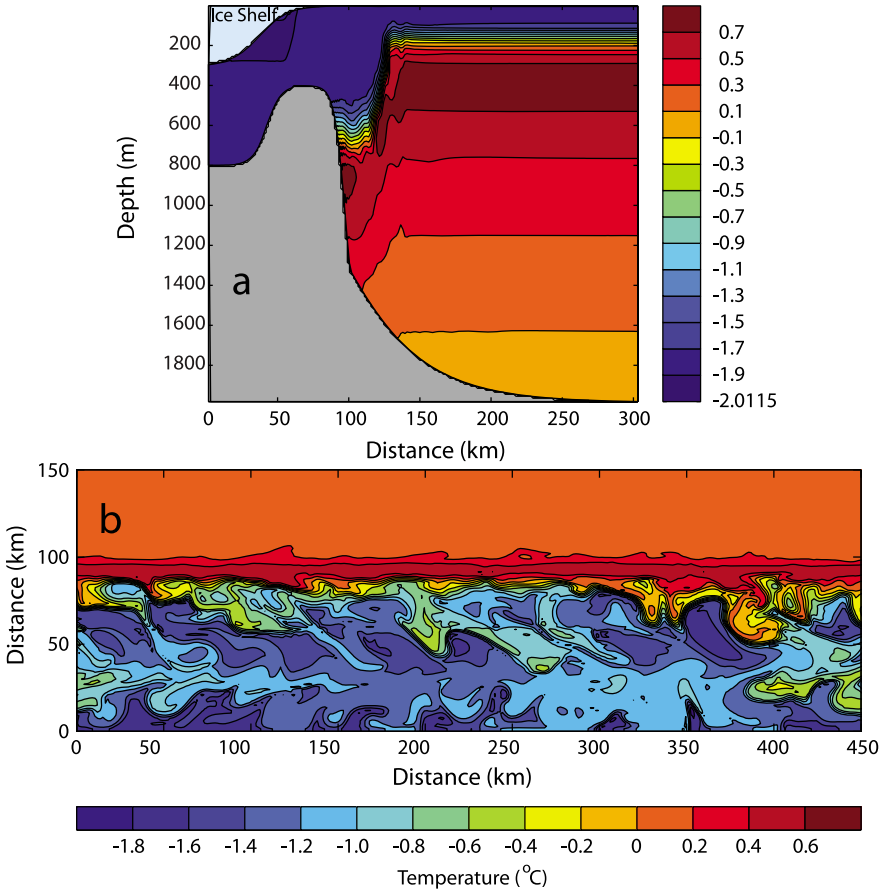

Figure 11. (a) The model's initial temperature field. (b) The bottom eddy-field after 135 days.

tion; (7) vertical mixing was parameterized by a general length scale (K-epsilon) mixing scheme [*Warner et al.*, 2005]; and (8) in order to permit eddies, the horizontal diffusion of tracers and momentum is turned off.

4.2. Results

[35] We run the model for constant (in time) westward winds of 3 ms^{-1}, 6 ms^{-1}, and 9 ms^{-1}, supplying surface stresses of 0.01, 0.04 and 0.08 Nm^{-2}. We do not attempt to simulate the frontal overturning in steady state, which would require intricate, and probably also unrealistic, restoring of water masses near the boundaries. Instead, we use the transient runs to illustrate the combined effect of the Ekman- and eddy overturning during the evolution of the frontal system. The simulations are integrated for 180 days, whereas all model runs show fully developed eddy fields after a spin-up period of 70 days.

[36] Figure 11b shows a snapshot of the bottom temperature after 135 days for the run forced with a constant 3 ms^{-1} wind. Eddies advect relatively warm water from the slope region into the ice shelf cavity. Modeled temperature profiles from beneath the ice shelf show a clear resemblance to the observed profile beneath the FIS (Figure 12). In the along-channel averaged temperature fields (Figure 13) relatively warm waters are advected into the ice shelf cavities in a near-bottom boundary layer in all runs except for the run forced with 9 ms^{-1} wind (Figures 13e and 13f). The inflow to the ice shelf cavities clearly gets weaker for stronger winds (Figures 13a–13f), and the inflow as seen in the temperature fields (Figures 13a, 13c and 13e) are clearly reflected by the residual velocities (Figures 13b, 13d and 13f). These are calculated following *McDougall and McIntosh* [2001], by computing along-channel averages of the transport within density layers. We first average one snapshot per day for days 121–135 days (choosing another time period, for instance day 165–180, gives qualitatively the same results) and then compute the mean of these 15 along-channel averages. Averaging on z-levels gives the Eulerian velocity field (Figure 14) which mainly shows the Ekman overturning. The inflow to the ice shelf cavity as seen from the residual overturning (Figure 13) occurs in the lower half of the water column, with a particularly intense flow near the bottom. The flow in the near-bottom boundary layer seems to steer modified WDW from the shelf break region into the cavity (this is most clearly seen in Figures 13a–13d), while the inflow higher in the water column mainly consists of water from above the thermocline and thus contains little heat. For strong winds (Figures 13e and 13f) the near-bottom boundary layer seems to be dominated by the bottom Ekman transport (Figure 14c), which effectively stops the inflow of modified WDW near the bottom.

[37] The Eulerian overturning is not in agreement with the advection of heat seen in Figure 13. The residual velocities

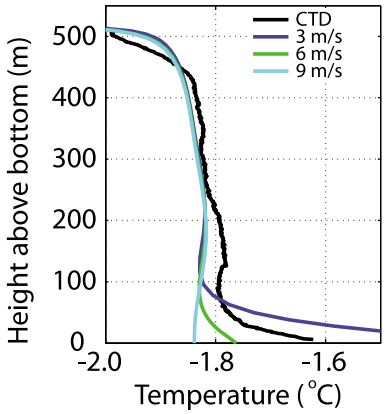

Figure 12. The observed temperature profile beneath the FIS (in black) and modeled temperature profiles (in colors) from the location shown by a vertical red line in Figures 13a, 13c and 13e.

include the eddy overturning and the direction of the residual velocities clearly match the advection of heat. The water masses flowing into the ice shelf cavity come from the shelf break or upper thermocline within the ASF. This is remarkably similar to the results of the data analysis (see section 3.3 and Figure 9). Since the difference between the Eulerian flow field and the residual flow field is the eddy overturning, the model results clearly show that the eddy overturning is important in advecting modified WDW onto the continental shelf and into the ice shelf cavities.

5. Discussion

[38] Onshore surface Ekman fluxes downwell when they meet the ice shelf front and create the ASF which acts as a barrier between the WDW and the continental shelf. Mesoscale eddies become essential in transporting modified WDW across the ASF, onto the continental shelf and into the ice shelf cavities in the EWS. This is supported by our combined analysis of hydrographic profiles collected by seal-borne instruments, the profile obtained by hot-water-drilling through the FIS, and the idealized modeling. Modified WDW is thus the source of ISW found below the FIS (Figure 9), and the flow of modified WDW onto the continental shelf drives basal ice shelf melting in the region. The downwelling surface water, the modified WDW crossing the ASF and glacial melting set the water mass properties on the shelf. In the following section we will discuss how

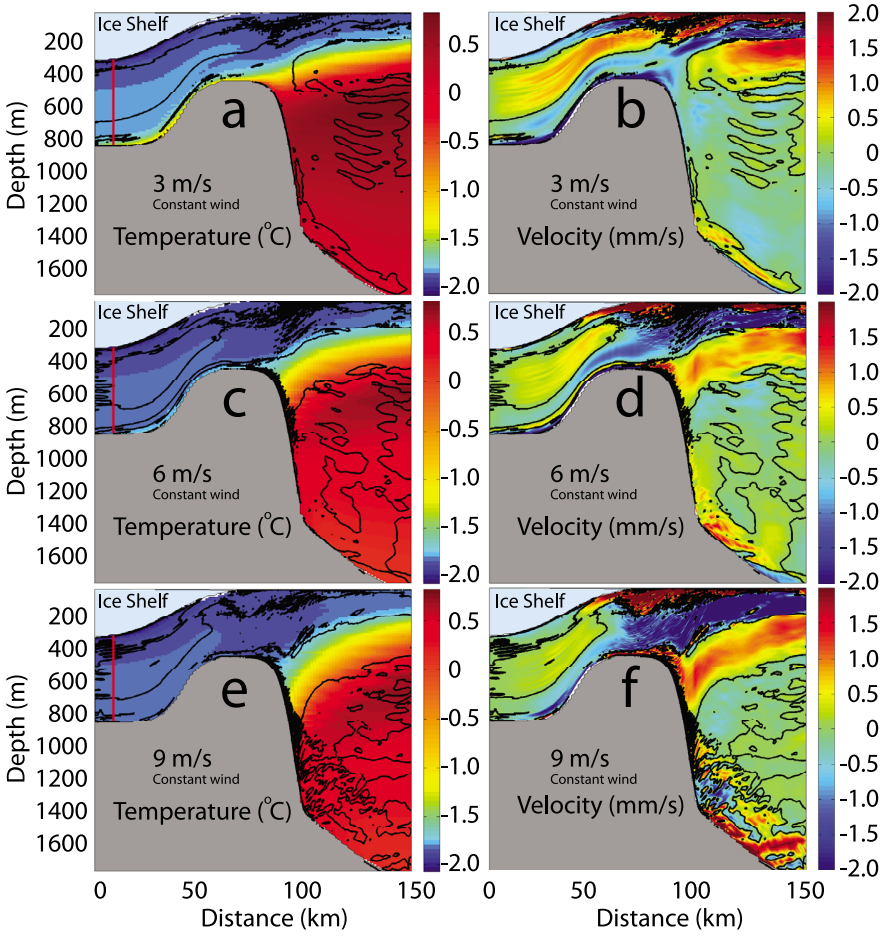

Figure 13. (a, c, e) The along-slope-averaged temperature and (b, d, f) the residual velocities estimated from daily snapshots from days 121–135. Negative velocities are to left. Contours of zero residual velocity are shown on top of the temperatures for easier comparison between velocity and temperature plots.

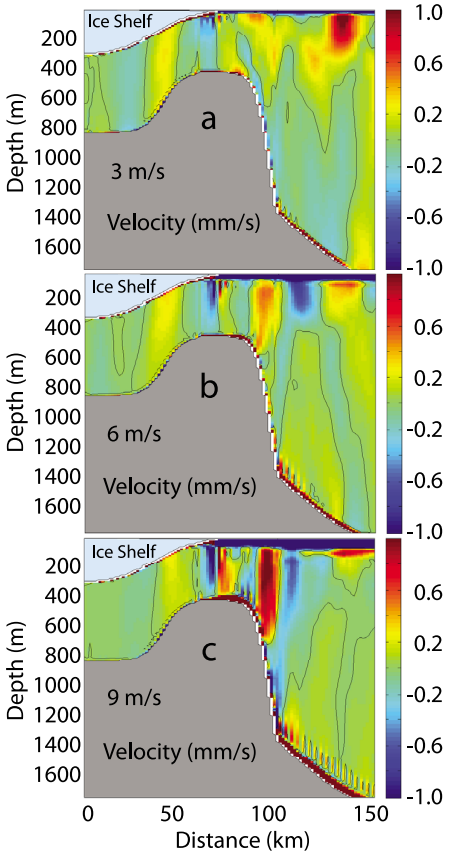

Figure 14. The Eulerian overturning velocities obtained by along-channel averaging at constant z-levels.

these processes interact and the consequences for formation of water masses, heat fluxes, heat budgets and glacial melting.

5.1. Formation of Low Salinity Shelf Waters

[39] The so-called Eastern Shelf Water (ESW), is a low salinity shelf water mass formed on the narrow shelves of the EWS. *Fahrbach et al.* [1994] conclude that basal ice shelf melting compensates for the combined effects of brine release induced by freezing and salinification from the WDW inflow. Our results indicate a somewhat different scenario, with onshore Ekman transport being the main process that acts to freshen the water masses south of the ASF (Figure 10). Since we ignored the melting caused by summer heat, glacial melting may have a larger effect, but this is not due to heat from the WDW. Since the modified WDW has a maximum temperature of about −1.5°C, the decrease in salinity due to interaction with ice shelves would be quite small. Actually, the lowest salinity that can be obtained by interaction between ice shelves and the modified WDW is given by S_{is} (equation (2)) (see *Gade* [1979] or *Nøst and Foldvik* [1994]), which is shown in Figure 8. S_{is} is higher than the depth-averaged salinity during most of the year, which shows that WDW cannot produce the low salinities observed on the shelf from February to August. Supporting the same argument, our observations also indicate lower sub–ice shelf temperatures than predicted by recent modeling studies of the EWS [*Smedsrud et al.*, 2006; *Thoma et al.*, 2006; *Nicholls et al.*, 2008b; *Thoma et al.*, 2010], which indicates less production of fresh surface water due to glacial melting than predicted by these models. *Hellmer* [2004] and *Beckmann and Goosse* [2003] reported model results showing that ice shelf melting has a strong impact on the salinity in the Weddell Sea, with consequences for sea ice and bottom-water formation. However, this might be a model artefact caused by unrealistically high temperatures for the WDW flowing onto the continental shelf.

[40] Our results suggest that the main reason that the low-salinity water occurs in the EWS is the freshening effect that onshore Ekman fluxes have on the shelf water masses (Figure 10). This effect depends on the surface-to-bottom salinity difference (equation (5)), which is largest in summer due to the fresh surface meltwater layer. This leads to strong seasonal variation in salinity, as can be seen in Figure 6. The Ekman transport is therefore a vital part of the process of forming the low salinity ESW, while the inflow of modified WDW will act to increase the salinity of the shelf waters, even after interacting with the ice shelves.

5.2. The Coastal Heat Budget and Glacial Melting

[41] We have based our data analysis on the salinity budget of the shelf waters. However, the salinity budget is intimately connected to the heat budget because freshwater is supplied to the ocean by melting of ice. After April, the temperature of the shelf waters are near freezing (Figure 6), and the net heat input relative to T_f must therefore be close to zero. The eddy overturning brings modified WDW onto the shelf and removes colder water higher in the water column. If all the inflowing modified WDW interacts with the ice shelf base it will be cooled to the freezing point. The heat relative to T_f will then be removed and the combined eddy and sub–ice shelf overturning will not add any heat to the shelf water masses. However, if the eddy overturning brings up more heat onto the continental shelf than that brought into contact with the ice shelf by the sub–ice shelf overturning (equivalent to $\gamma < 1$), heat will be added to the water column that will increase the temperature of the shelf waters. This is probably the most realistic situation, and from the modeled residual velocities (Figure 13) we clearly see that the overturning is stronger in the open ocean than under the ice shelf. But despite this, the modeled temperatures of the shelf water masses do not increase during the 135 days after initialization (Figure 11). The reason for this is probably that a large part of the inflowing water comes from above the thermocline (see Figure 13). Thus, the flow onto the shelf consists of cold near-surface water and relatively warm modified WDW near the bottom, but the mean temperature of the inflowing water is probably not much higher than the mean temperature of the outflowing water. The net increase in heat content is therefore probably small even when some of the modified WDW does not interact with the ice shelf. Based on this the heat budget for winter seems to be in balance. The heat flux to the atmosphere does not affect the ocean because this is heat released by formation of sea ice.

[42] In February and March the summer heat contained in the water column must be removed. As seen in Figure 6 this heat is removed within a period of about one month, which

requires a heat flux of about 100 W/m^2 if the heat escapes through the sea surface. The estimated surface heat flux (see Appendix A2) is mostly negative (representing an ocean heat gain) in February, but reaches about 100 W/m^2 in mid March. However, sea ice formation starts in March (see Appendix A2) and much of the surface heat loss will therefore not cool the ocean. Thus, it is not likely that the observed cooling in March is caused by the surface heat loss alone. Interaction with the ice shelf is probably also contributing to the cooling. This will also add freshwater to the ocean waters, which will lead to a more realistic result than the freshening eddy overturning effect in March shown in Figure 10. The conclusion from this is that the heat budget seems to be consistent with the exchange processes and rates estimated from the salinity budget.

[43] Theoretically it is possible to find the eddy overturning values (V_{eo}) from the salinity budget terms (Figure 10) and multiply them with observed temperatures to find the heat fluxes towards the ice shelves, which again can be used to estimate melt rates. We have estimated the melt rates from our data to be in the order of 1 m/yr, assuming the DML ice-shelves cover an area of 100,000 km^2. The uncertainties in these melt rate estimates are huge (in the order of 100 %), but melt rates obtained from the estimated exchange across the ASF are within realistic frames, which is reassuring. The major goal of this work was not to estimate melt rates, but rather to reveal some of the complicated processes involved in transporting heat towards the ice-shelves in the EWS.

5.3. Heat Fluxes Towards the Ice Shelves

[44] Except for solar heating during summer, the only heat source for glacial melting is the WDW, and it is brought onto the continental shelf by eddy-overturning of the ASF. The hydrographic profile obtained from beneath FIS and the idealized numerical model both show that the modified WDW enters the ice shelf cavity in a boundary layer near the seabed (Figures 12 and 13). In the ocean interior, eddy fluxes tend to be directed along isopycnals, whereas near the seabed or the surface, they are forced along the boundaries. In the case of the ASF, isopycnals intersect the seabed and the southward isopycnal eddy fluxes are directed towards the seabed where they are forced to flow along the bottom. Thus, the intersection between isopycnals and the seabed near the shelf break might drive the flow in the near-bottom boundary layers. Eddy transports near surface and bottom boundary layers have been the topic of many studies [*Treguier et al.*, 1997; *Ferrari et al.*, 2008, 2010], and there are also studies on eddy fluxes over sloping seabeds [*Greatbatch and Li*, 2000; *Adcock and Marshall*, 2000; *Isachsen*, 2010]. We have shown that eddy fluxes are important in bringing modified WDW onto the continental shelf in the EWS, but further work is needed to understand the characteristics of the eddy fluxes in this region.

[45] Figure 13 shows that the overturning circulation in the open ocean increases in magnitude with increasing wind forcing, while the overturning beneath the ice shelf decreases with increasing wind. The wind forcing is zero below the ice shelf and the thermodynamic forcing at the ice shelf base (which forces the circulation under the ice shelf) is driven by inflow of heat, which is strongest for weak winds. The water that is available on the shelf is circulated beneath the ice shelf as part of the sub–ice shelf overturning. Above we concluded that sub–ice shelf melting can not cause the low salinities characterizing the low salinity shelf water found along the coast of DML. However, the buoyancy input due to glacial melting may still play a central role in the dynamics causing WDW to access the shelf and the ice shelf cavities. To understand this we assume a steady state and follow the theory developed for the ACC by *Marshall and Radko* [2003]. Lets first consider a circulation that is purely wind driven, with no mixing and no buoyancy input. In this case downwelling due to the onshore surface Ekman flux will create the ASF. This will build up the potential energy in the system which will be released by baroclinic instability of the ASF. If all the energy input by the downwelling Ekman transport is released, the front will be stationary with an eddy overturning exactly balancing the Ekman overturning leading to zero residual flow. With the assumptions made, only advection can change the water mass structure, and the steady state solution is therefore no flow. An eddy overturning supplying WDW to the continental shelf is then impossible since this will require a non-zero residual transport and a release of potential energy which is larger than the potential energy supplied by the downwelling Ekman transport. When buoyancy is supplied or removed, thus transforming water masses, the situation is different; advection is now needed to balance the input or loss of buoyancy. Basal ice shelf melting is an extra source of buoyancy on the shelf which will transform water masses and increase the potential energy further. In a steady state, the residual transport will remove the buoyancy supplied by the glacial melting. This is achieved by an eddy overturning which is slightly larger than the Ekman overturning, driven by baroclinic instability releasing the potential energy supplied by the glacial melting in addition to the energy supplied by downwelling Ekman transport. Thus, glacial melting as a source of buoyancy on the shelf is needed for a residual circulation to advect WDW onto the continental shelf. In our simplified numerical model the effect is clear; when thermodynamics under the ice shelf is turned off, the modified WDW does not flow onto the shelf (this simulation is not shown). So even though the freshwater input by basal melting can not create the low salinity shelf waters, it is still a central process in the interaction between ice shelf cavities, continental shelves and the deep ocean. In one way the inflow of WDW is maintaining itself by being the heat source driving melting beneath the ice shelves.

6. Conclusion

[46] We analyze 2351 new hydrographic profiles collected along the Antarctic Coast in the EWS collected by southern elephant seals in 2008, and a profile obtained by hot-water-drilling through the FIS in 2009. Exchanges across the ASF are estimated using parameters derived from the data in a conceptual model of the exchange processes. From this we conclude that eddy overturning of the ASF brings WDW onto the continental shelf and into the ice shelf cavities. The conclusion is supported by the results from an eddy-resolving numerical ice shelf–ocean model. This model shows that eddy overturning of the ASF brings WDW onto the continental shelf and into the ice shelf cavity within a

boundary layer near the seabed. The modeled water mass structure with a near bottom layer of modified WDW shows striking agreement with the observed temperature profile beneath the FIS.

[47] We find that the main process causing low-salinity shelf waters to be formed in the EWS is the onshore surface Ekman fluxes. This drives fresher waters towards the shelf, and is a vital part of the process of forming the low salinity EWS. The inflow of modified WDW will, contradictory to earlier suggestions [*Fahrbach et al.*, 1994], act to increase the salinity of the shelf waters, even after interacting with the ice shelves. The freshwater input due to basal melting of ice shelves can not form the low salinites observed on the shelf because the temperature of the modified WDW flowing into the cavities are too low. However, despite this, the glacial melting is still a vital factor in the exchange of modified WDW across the ASF. The buoyancy input and water mass transformation by glacial melting leads to a residual overturning of the ASF that transports modified WDW onto the shelf and into the cavities.

[48] The importance of mesoscale eddies to transport heat towards the ice shelves in the EWS is clearly illustrated in this study. The ASF is a continuous feature throughout the central and western Pacific, Indian and Atlantic sectors of the Southern Ocean, and it is instrumental in the formation of modified WDW [*Whitworth et al.*, 1998]. It is highly likely that mesoscale eddies created by baroclinic instability is important for the formation of modified WDW along the whole length of the ASF. Mesoscale eddy transport, especially over sloping topography, is poorly understood. Given the importance of ocean heat fluxes for ice shelf basal melt rates, further work towards an understanding of mesoscale eddies over sloping topography is essential.

Appendix A: Estimating Variables and Their Uncertainties From Data

[49] In order to estimate the salt fluxes that make up equation (8), we need to estimate the variables included (and their affiliated uncertainties) from data.

A1. Parameters Derived From Hydrographic Data

[50] We estimate S_{da}, S_s, S_b, S_w and T_w from the hydrographic data. S_w and T_w are estimated from the analysis in the TS diagram presented in Figure 9 and S_m from equation (4). Salinity as a function of time and pressure (Figure 6) and its uncertainties are estimated in the following way. The uncertainty of the mean salinity within each time-pressure bin (see section 2.2) is given by [*Taylor*, 1982]

$$\delta_{n,k} = \frac{\sigma_{n,k}}{\sqrt{N_{n,k}}}, \tag{A1}$$

where $\delta_{n,k}$ is the uncertainty, $\sigma_{n,k}$ is the standard deviation and $N_{n,k}$ is the number of observations within each bin marked by the time index n and pressure index k. The number of observations and standard deviation of the salinity within each bin is shown in Figure 4. We then assume that the observations within each bin are independent and subject to random errors.

[51] The depth averaged salinity, S_{da}, and its uncertainty, δ_{da}, are estimated as follows:

$$S_{da} = \frac{1}{\Delta p}\sum_{k=k_b}^{k_s} S_{n,k} dp_{n,k} \tag{A2}$$

$$\delta_{da} = \frac{1}{\Delta p}\sqrt{\sum_{k=k_b}^{k_s} \left(\delta_{n,k} dp_{n,k}\right)^2}, \tag{A3}$$

where S_n is the salinity within each bin, Δp is the total surface to bottom pressure difference, dp is the pressure difference over each bin and the indexes k_b and k_s marks the upper and lower bins. The depth-averaged salinity and its uncertainty are plotted in Figure 8. When deriving the uncertainty of the depth-averaged salinity (equation (A3)) we use classical theory for error analysis and propagation of uncertainties [*Taylor*, 1982]. This is done throughout the paper when estimating uncertainties for the different terms.

[52] The surface salinity, S_s, and its uncertainty, δ_s, are set equal to the salinity and uncertainty in the upper pressure bin:

$$S_s = S_{n,k_s} \tag{A4}$$

and

$$\delta_s = \delta_{n,k_s}. \tag{A5}$$

Similarly, the near-bottom salinity, S_b, and its uncertainty, δ_b, are given by the salinity and uncertainty in the lowermost bin:

$$S_b = S_{n,k_b} \tag{A6}$$

and

$$\delta_b = \delta_{n,k_b}. \tag{A7}$$

S_s and S_b with their corresponding uncertainties are both plotted in Figure 8.

[53] The time derivative of the depth-averaged salinity is calculated by first using a straight forward difference between two neighboring time bins and then using a running mean within a 30-day window. This can be expressed as follows:

$$\frac{dS_{da}}{dt} = \frac{1}{2n_w dt}\sum_{j=n-n_w}^{n+n_w}\left(S_{da}|_{j+1} - S_{da}|_j\right), \tag{A8}$$

where $n_w = 15$ and the time step, dt, equals one day. The uncertainty in this time derivative is given by

$$\delta_t = \frac{1}{2n_w dt}\sqrt{\sum_{j=n-n_w}^{n+n_w}\left(\delta^2_{da}|_{j+1} + \delta^2_{da}|_j\right)}. \tag{A9}$$

A2. Estimating Salt Input Due to Sea Ice Formation

[54] To estimate the salt input due to sea ice formation, we need to estimate the surface heat loss. First, we esti-

mate the heat loss from an open ocean surface, which is given by

$$Q_{tot} = Q_s + Q_l + Q_r. \tag{A10}$$

Q_{tot} is the total heat flux, Q_s is the sensible heat flux, Q_l is the latent heat flux and Q_r is the net radiative heat flux. Meteorological data from NCEP, sea surface temperatures collected by the seal-borne instruments and exchange coefficients [*DeCosmo et al.*, 1996] are used as input to bulk formulas [*Smith*, 1988] for Q_s and Q_l. Q_r is given by a balance between downward longwave and shortwave radiation from NCEP data, and upward longwave radiation given by Stefan's law with sea surface temperatures as input. Upward shortwave radiation is set to zero as ocean water has an albedo near zero. The area of open water within a distance W of the ice front/coast is determined from the AMSR-E sea ice concentrations. Heat loss from the ice-covered area is set to 5 Wm^{-2} based on data from the Weddell Sea [*Vihma et al.*, 2002]. The heat loss within an area $A = A_o + A_i$, where A_o is the area of open water and A_i is the ice-covered area, is then given by

$$Q = \frac{Q_{tot}A_o + 5A_i}{A}. \tag{A11}$$

[55] The uncertainty, δ_Q, of the surface heat loss, Q, is difficult to estimate accurately. However, the NCEP data, used to estimate Q, agree quite well with meteorological data from the German Neumayer Station (70°39′S, 8°15′W), which makes us believe that our estimates of Q are reasonable. Accuracies of the sea ice concentrations data, the sea surface temperatures data and the underlying theoretical model additionally determine uncertainty levels. Our uncertainty estimates can therefore be seen as a guess. However, we believe the uncertainty is less than 20 percent and therefore we set

$$\delta_Q = 0.2Q. \tag{A12}$$

[56] From the AMSR-E sea ice concentrations we see that sea ice starts forming around 1 March and by 1 April the coastal areas are covered by sea ice. Additionally, by the 1st of April the water column on the shelf was cooled to temperatures near freezing. Based on this, we set $\alpha = 0$ before 1 March. After 1 April we set $\alpha = 1$, and between 1 March and 1 April we let α vary linearly from zero to one. We believe that this is accurate after 1 April. In March α is uncertain, but brine release due to sea ice formation does not play a significant role during this period and therefore, we do not specify any uncertainty connected to α. Newly formed sea ice will contain some salt [*Smedsrud and Skogseth*, 2006; *Notz and Worster*, 2008], and we set the salinity in the ice as

$$S_i = 10 \pm \delta_i, \tag{A13}$$

where δ_i is set to 5 psu.

[57] The rate of change of salt within the specified volume is then given by

$$WH\left(\frac{dS_{da}}{dt}\right)_{if} = \alpha\frac{WQ}{\rho L}(S_{da} - S_i), \tag{A14}$$

which equals the rightmost term in equation (8). The uncertainty connected to this term is given by

$$\delta_{if} = WH\left(\frac{dS_{da}}{dt}\right)_{if}\sqrt{\left(\frac{\delta_i}{S_{da} - S_i}\right)^2 + \left(\frac{\delta_W}{W}\right)^2 + \left(\frac{\delta_Q}{Q}\right)^2}. \tag{A15}$$

The uncertainty in $(S_{da} - S_i)$ is dominated by the uncertainty in δ_i, and therefore, S_i can be ignored in this expression. Equations (A14) and (A15) are used when plotting the contribution of sea ice formation to the salinity budget (Figure 10).

A3. Ekman Transport

[58] The Ekman transport, V_{ek}, is determined from stresses at the ocean surface. We first estimate the stress between the air and the combined ocean/sea ice surface:

$$\tau_c = \rho_a C_{Da}\sqrt{U^2 + V^2}U_c. \tag{A16}$$

ρ_a is the density of air, τ_c is the eastward alongshore wind stress, U and V are the eastward and northward 10 m wind speed from NCEP and U_c is its alongshore component. The drag coefficient, C_{Da}, is represented as a function of the sea ice concentration, Ic:

$$C_{Da} = 1.89 \cdot 10^{-3}Ic + 1.25 \cdot 10^{-3}(1 - Ic), \tag{A17}$$

where values for the drag coefficient in neutral stratification over the ocean ($1.25 \cdot 10^{-3}$) and sea ice ($1.89 \cdot 10^{-3}$) are used [*Lüpkes and Birnbaum*, 2005]. We do not take into account the stability of the atmosphere because we consider the effect of this to be small compared to the uncertainties related to the effect of the sea ice cover. When sea ice concentrations are lower than 0.8, we assume that equations (A16) and (A17) also describe the stress at the ocean surface, because the internal forces within the ice cover are then considered small and the air-ice stress is then assumed to be transferred to the ocean. However, for ice concentrations higher than 0.8, some of the air-ice stress will be balanced by internal stresses in the ice [*Uotila et al.*, 2000] and the ice-ocean stress will be reduced. Because we do not have detailed information about the ice dynamics we have to make some quite rough assumptions. In the case of ice concentrations above 0.8, we assume that the stress on the ocean surface will be half of the stress given by equations (A16) and (A17). In short, we represent the stress on the ocean surface by equation (A16) with C_{Da} replaced by C_D, with our assumption about the relation between ice-ocean and air-ice stress incorporated in C_D. This gives

$$\tau = \rho_a C_D\sqrt{U^2 + V^2}U_c, \tag{A18}$$

where $C_D = C_{Da}/2$ for $Ic > 0.8$, while $C_D = C_{Da}$ for $Ic \leq 0.8$. The Ekman transport is now given by

$$V_{ek} = \frac{\tau}{\rho_0 f}, \tag{A19}$$

where ρ_0 is a reference ocean density while f is the Coriolis parameter. Due to our limited information about the effect of sea ice, uncertainties are large.

[59] The drag coefficient over sea ice depends on sea ice characteristics as well as sea ice concentrations [*Lüpkes and Birnbaum*, 2005], and in addition, internal stress in the pack ice might balance a significant part of the air-ice stress [*Uotila et al.*, 2000] during periods of high ice concentrations. Because of this, the estimation of Ekman transport is highly uncertain. We assume that when ice concentrations are above 0.8 internal forces in the ice might play a significant role. However, because the internal forces in the ice are as yet unknown we set a higher uncertainty when ice concentrations are higher than 0.8. For ice concentrations below 0.8 we set the uncertainty to $\delta_e = 0.2V_{ek}$, while for ice concentrations above 0.8 we set it to $\delta_e = 0.5\ V_{ek}$.

A4. The Salinity Budget and Uncertainties

[60] The first term, $WHdS_{da}/dt$, can be found by multiplying equation (A8) with W and H. Its uncertainty is given by

$$\delta_1 = WH\frac{dS_{da}}{dt}\sqrt{\left(\frac{\delta_W}{W}\right)^2+\left(\frac{\delta_H}{H}\right)^2+\left(\frac{\delta_t}{\frac{dS_{da}}{dt}}\right)^2}, \tag{A20}$$

where δ_t is given by equation (A9). The salt input due to sea ice formation and its uncertainty are given by equations (A14) and (A15). Uncertainties in the Ekman transport term, $V_{ek}(S_s - S_b)$, are given by

$$\delta_E = V_{ek}(S_s - S_b)\sqrt{\left(\frac{\delta_e}{V_{ek}}\right)^2+\frac{\delta_s^2+\delta_b^2}{(S_s-S_b)^2}}. \tag{A21}$$

The eddy overturning term, $V_{eo}(S_{da} - S_m)$, can then be determined from equation (8) as it is the only unknown. Its uncertainty is given by

$$\delta_{ot} = \sqrt{\delta_1^2+\delta_{if}^2+\delta_E^2}. \tag{A22}$$

[61] **Acknowledgments.** We thank Keith Nicholls and Keith Makinson for the loan of hot-water-drilling equipment and assistance with preparations for field work. We also thank Eberhard Fahrbach and Gerd Rohardt for letting us use CTD data from the 2008 Polarstern cruise for calibrating the seal CTD data. The Argo data that were used for calibrating the data collected by the seals were collected and made freely available by the International Argo Project and the national programs that contribute to it. (http://www.argo.ucsd.edu, http://argo.jcommops.org). Argo is a pilot program of the Global Ocean Observing System. This work was supported by the Norwegian Polar Institute's Centre for Ice, Climate and Ecosystems (ICE) and by the Norwegian Antarctic Research Expeditions (NARE).

References

Adcock, S. T., and D. P. Marshall (2000), Interactions between geostrophic eddies and the mean circulation over large-scale bottom topography, *J. Phys. Oceanogr.*, *30*, 3223–3238.

Aiki, H., T. Jacobson, and T. Yamagata (2004), Parameterizing ocean eddy transports from surface to bottom, *Geophys. Res. Lett.*, *31*, L19302, doi:10.1029/2004GL020703.

Amante, C., and B. W. Eakins (2008), ETOPO1 1 Arc-Minute Global Relief Model: Procedures, data sources and analysis, *Tech. Memo NESDIS NGDC*-24, National Geophysical Data Center, U.S. Dep. of Commer., Boulder, Colo.

Andrews, D. G., J. R. Holton, and C. B. Leovy (1987), *Middle Atmosphere Dynamics*, *Int. Geophys. Ser.*, vol. 40, Academic, Orlando, Fla.

Beckmann, A., and H. Goosse (2003), A parameterization of ice shelf-ocean interaction for climate models, *Ocean Modell.*, *5*, 157–170.

Biuw, M., et al. (2007), Variations in behavior and condition of a southern ocean top predator in relation to in situ oceanographic conditions, *Proc. Natl. Acad. Sci.*, *104*(34), 13,705–13,710.

Charrassin, J. B., et al. (2008), Southern ocean frontal structure and sea-ice formation rates revealed by elephant seals, *Proc. Nat. Acad. Sci.*, *105*(33), 11,634–11,639.

Chavanne, C. P., K. J. Heywood, K. W. Nicholls, and I. Fer (2010), Observations of the Antarctic slope undercurrent in the southeastern Weddell Sea, *Geophys. Res. Lett.*, *37*, L13601, doi:10.1029/2010GL043603.

Deacon, G. E. R. (1979), The Weddell Gyre, *Deep Sea Res.*, *26A*, 981–995.

DeCosmo, J., K. B. Katsaros, S. D. Smith, R. J. Anderson, W. A. Oost, K. Bumke, and H. Chadwick (1996), Air-sea exchange of water vapor and sensible heat: The humidity exchange over the sea (HEXOS) results, *J. Geophys. Res.*, *101*, 12,001–12,016.

Dinniman, M., J. M. Klinck, and W. O. Smith Jr. (2007), Influence of sea ice cover and icebergs on circulation and water mass formation in a numerical circulation model of the Ross Sea, Antarctica, *J. Geophys. Res.*, *112*, C11013, doi:10.1029/2006JC004036.

Fahrbach, E., G. Rohardt, and G. Krause (1992), The Antarctic Coastal Current in the southeastern Weddell Sea, *Polar Biol.*, *12*(2), 171–182.

Fahrbach, E., R. G. Peterson, G. Rohardt, P. Schlosser, and R. Bayer (1994), Suppression of bottom water formation in the south-eastern Weddell Sea, *Deep Sea Res.*, *41*, 389–411.

Fedak, M. A., S. S. Anderson, and M. G. Curry (1983), Attachment of a radio tag to the fur of seals, *J. Zool.*, *200*, 298–300.

Ferrari, R., J. C. McWilliams, V. M. Canuto, and M. Dubovikov (2008), Parameterization of eddy fluxes near oceanic boundaries, *J. Clim.*, *321*, 2770–2789.

Ferrari, R., S. M. Griffies, A. J. G. Nurser, and G. K. Vallis (2010), A boundary-value problem for the parameterized mesoscale eddy transport, *Ocean Modell.*, *32*, 143–156.

Gade, H. (1979), Melting of ice in sea water: a primitive model with application to the Antarctic ice shelf and ice bergs, *J. Phys. Oceanogr.*, *9*, 189–198.

Gent, P. R., and J. C. McWilliams (1990), Isopycnal mixing in ocean circulation models, *J. Phys. Oceanogr.*, *20*, 150–155.

Gill, A. E. (1973), Circulation and bottom water production in the Weddell Sea, *Deep Sea Res.*, *20*, 111–140.

Gould, J., et al. (2004), Argo profiling floats bring new era of in situ ocean observations, *Eos Trans. AGU*, *85*(19), 450–457.

Greatbatch, R. J., and G. Li (2000), Alongslope mean flow and an associated upslope bolus flux of tracer in a parameterization of mesoscale turbulence, *Deep Sea Res.*, *47*, 709–735.

Hellmer, H. H. (2004), Impact of Antarctic ice shelf basal melting on sea ice and deep ocean properites, *Geophys. Res. Lett.*, *31*, L10307, doi:10.1029/2004GL019506.

Heywood, K. J., R. A. Locarnini, R. D. Frew, P. F. Dennis, and B. A. King (1998), Transport and water masses of the Antarctic Slope Front system in the eastern Weddell Sea, in *Ocean, Ice and Atmosphere: Interactions at the Antarctic Continental Margin*, *Antarct. Res. Ser.*, vol. 75, edited by S. S. Jacobs and R. F. Weiss, pp. 203–214, AGU, Washington D. C.

Holland, D. M., R. H. Thomas, B. DeYoung, M. H. Ribergaard, and B. Lyberth (2008), Acceleration of Jakobshavn Isbræ triggered by warm subsurface ocean waters., *Nat. Geosci.*, *1*, 659–664, doi:10.1038/NGEO316.

Isachsen, P. E. (2010), Baroclinic instability and eddy tracer transport across sloping bottom topography: How well does a modified Eady model do in primitive equation simulations?, *Ocean Modell.*, *39*(1–2), 183–199, doi:10.1016/j.ocemod.2010.09.007.

Jackett, D. R., T. J. McDougall, R. Feistel, D. G. Wright, and S. M. Griffies (2006), Algorithms for density, potential temperature, conservative temperature, and the freezing temperature of seawater, *J. Atmos. Oceanic Technol.*, *23*, 1709–1728.

Kalnay, E., et al. (1996), The NCEP/NCAR 40-year reanalysis project, *Bull. Am. Meteorol. Soc.*, *77*(3), 437–471.

Lüpkes, C., and G. Birnbaum (2005), Surface drag in the arctic marginal sea-ice zone: A comparison of different parameterization concepts, *Boundary Layer Meteorol.*, *117*, 179–211.

Marshall, J., and T. Radko (2003), Residual-mean solutions for the Antarctic Circumpolar Current and its associated overturning circulation, *J. Phys. Oceanogr.*, *33*(11), 2341–2354.

McDougall, T. J., and P. C. McIntosh (2001), The temporal-residual-mean velocity. Part II: Isopycnal interpretation and the tracer and momentum equations, *J. Phys. Oceanogr.*, *31*, 1222–1246.

Nicholls, K. W., et al. (2006), Measurements beneath an Antarctic ice shelf using an autonomous underwater vehicle, *Geophys. Res. Lett.*, *33*, L08612, doi:10.1029/2006GL025998.

Nicholls, K. W., L. Boehme, M. Biuw, and M. A. Fedak (2008a), Wintertime ocean conditions over the southern weddell sea continental shelf, antarctica, *Geophys. Res. Lett.*, *35*, L21605, doi:10.1029/2008GL035742.

Nicholls, K. W., E. P. Abrahamsen, K. J. Heywood, K. Stansfield, and S. Østerhus (2008b), High-latitude oceanography using autosub autonomous underwater vehicle, *Limnol. Oceanogr.*, *53*(5), 2309–2320.

Nøst, O. A. (2004), Measurements of ice thickness and seabed topography under the Fimbul Ice Shelf, Dronning Maud Land, Antarctica, *J. Geophys. Res.*, *109*, C10010, doi:10.1029/2004JC002277.

Nøst, O. A., and A. Foldvik (1994), A model of ice shelf ocean interaction with application to the Filchner Ronne and Ross ice shelves, *J. Geophys. Res.*, *99*, 14,243–14,254.

Nøst, O. A., and P. E. Isachsen (2003), The large-scale time-mean ocean circulation in the Nordic Seas and Arctic Ocean estimated from simplified dynamics, *J. Mar. Res.*, *61*, 175–210.

Nøst, O. A., and T. Lothe (1997), The Antarctic Coastal Current – physical oceanographic results from NARE 1996/97, in *Norsk Polarinstitutt Meddelelser*, vol. 148, edited by J. G. Winther, pp. 51–57, Norsk Polarinstitutt, Tromso, Norway.

Notz, D., and M. G. Worster (2008), In situ measurements of the evolution of young sea ice, *J. Geophys. Res.*, *113*, C03001, doi:10.1029/2007JC004333.

Nunez-Riboni, I., and E. Fahrbach (2009), Seasonal variability of the Antarctic Coastal Current and its driving mechanisms in the Weddell Sea, *Deep Sea Res., Part I*, *56*, 1927–1941.

Ohshima, K. I., T. Takizawa, S. Ushio, and T. Kawamura (1996), Seasonal variations of the Antarctic coastal ocean in the vicinity of Lützow-Holm Bay, *J. Geophys. Res.*, *101*(C9), 20,617–20,628.

Owens, W. B., and A. P. S. Wong (2009), An improved calibration method for the drift of the conductivity sensor on autonomous CTD profiling floats by θ-S climatology, *Deep Sea Res., Part I*, *56*, 450–457.

Pollard, D., and R. M. DeConto (2009), Modelling West Antarctic ice sheet growth and collapse through the past five million years, *Nature*, *458*, doi:10.1038/nature07809.

Price, M. R., K. J. Heywood, and K. W. Nicholls (2008), Ice-shelf-ocean interactions at Fimbul Ice Shelf, Antarctica from oxygen isotope ratio measurements, *Ocean Sci.*, *4*, 89–98.

Rintoul, S. R., C. Hughes, and D. Olbers (2001), The Antarctic Circumpolar Current System, in *Ocean Circulation and Climate*, *Int. Geophys. Ser.*, vol. 77, chap. 4.6, pp. 271–302, Academic, New York.

Shchepetkin, A. F., and J. C. McWilliams (2005), The Regional Ocean Modeling System (ROMS): A split-explicit, free-surface, topography-following coordinates ocean model, *Ocean Modell.*, *9*, 347–404.

Shepherd, A., D. J. Wingham, and A. D. Mansley (2002), Inland thinning of the Amundsen Sea sector, West Antarctica, *Geophys. Res. Lett.*, *29*(10), 1364, doi: 10.1029/2001GL014183.

Smedsrud, L. H., and R. Skogseth (2006), Field measurements of Arctic grease ice properties and processes, *Cold Reg. Sci. Tech.*, *44*, 171–183.

Smedsrud, L. H., A. Jenkins, D. M. Holland, and O. A. Nøst (2006), Modeling ocean processes below Fimbulisen, Antarctica, *J. Geophys. Res.*, *111*, C01007, doi:10.1029/2005JC002915.

Smith, S. D. (1988), Coefficients for sea surface wind stress, heat flux, and wind profiles as a function of wind speed and temperature, *J. Geophys. Res.*, *93*(C12), 15,467–15,472.

Spreen, G., L. Kaleschke, and G. Heygster (2008), Sea ice remote sensing using AMSR-E 89 GHz channels, *J. Geophys. Res.*, *113*, C02S03, doi:10.1029/2005JC003384.

Straneo, F., G. S. Hamilton, D. A. Sutherland, L. A. Stearns, F. Davidson, M. O. Hammill, G. B. Stenson, and A. Rosing-Asvid (2010), Rapid circulation of warm subtropical waters in a major glacial fjord in East Greenland, *Nat. Geosci.*, *3*, 182–186, doi:10.1038/NGEO764.

Sverdrup, H. U. (1953), The currents off the coast of Queen Maud Land, *Nor. Geol. Tidsskr.*, *14*, 239–249.

Taylor, J. R. (1982), *An Introduction to Error Analysis: The Study of Uncertainties in Physical Measurements*, Univ. Sci. Books, Mill Valley, Calif.

Thoma, M., K. Grosfeld, and M. A. Lange (2006), Impact of the Eastern Weddell Sea ice shelves on water masses in the eastern Weddell Sea, *J. Geophys. Res.*, *111*, C12010, doi:10.1029/2005JC003212.

Thoma, M., A. Jenkins, D. Holland, and S. S. Jacobs (2008), Modeling circumpolar deep water intrusions on the Amundsen Sea continental shelf, *Geophys. Res. Lett.*, *35*, L18602, doi:10.1029/2008GL034939.

Thoma, M., K. Grosfeldt, K. Makinson, and M. A. Lange (2010), Modelling the impact of ocean warming on melting and water masses of ice shelves in the Eastern Weddell Sea, *Ocean Dyn.*, *60*, 479–489, doi:10.1007/s10236-010-0262-x.

Treguier, A. M., I. M. Held, and V. D. Larichev (1997), Parameterization of quasigeostrophic eddies in primitive equation ocean models, *J. Phys. Oceanogr.*, *27*, 567–580.

Tverberg, V., and O. A. Nøst (2009), Eddy overturning across a shelf edge front: Kongsfjorden, West Spitsbergen, *J. Geophys. Res.*, *114*, C04024, doi:10.1029/2008JC005106.

Uotila, J., T. Vihma, and J. Launiainen (2000), Response of the Weddell Sea pack ice to wind forcing, *J. Geophys. Res.*, *105*, 1135–1151.

Vihma, T., J. Uotila, B. Cheng, and J. Launiainen (2002), Surface heat budget over the Weddell Sea: Buoy results and model comparisons, *J. Geophys. Res.*, *107*(C2), 3013, doi:10.1029/2000JC000372.

Wåhlin, A. K., X. Yuan, G. Björk, and C. Nohr (2010), Inflow of warm Circumpolar Deep Water in the central Amundsen shelf, *J. Phys. Oceanogr.*, *40*, 1427–1434, doi:10.1175/2010JPO4431.1.

Walker, D. P., M. A. Brandon, A. Jenkins, J. T. Allen, J. A. Dowdeswell, and J. Evans (2007), Oceanic heat transport onto the Amundsen Sea shelf through a submarine glacial trough, *Geophys. Res. Lett.*, *34*, L02602, doi:10.1029/2006GL028154.

Warner, J. C., C. R. Sherwood, H. G. Arango, and R. P. Signell (2005), Performance of four turbulence closure methods implemented using a generic length scale method, *Ocean Modell.*, *8*, 81–113.

Whitworth, T., A. H. Orsi, S. J. Kim, W. D. Nowlin, and R. A. Locarnini (1998), Water masses and mixing near the Antarctic Slope Front, in *Ocean, Ice and Atmosphere: Interactions at the Antarctic Continental Margin*, *Antarct. Res. Ser.*, vol. 75, edited by S. S. Jacobs and R. F. Weiss, pp. 1–27, AGU, Washington D. C.

M. Biuw, T. Hattermann, K. M. Kovacs, C. Lydersen, O. A. Nøst, V. Tverberg, and Q. Zhou, Norwegian Polar Institute, Fram Center, N-9296 Tromsø, Norway. (ole@npolar.no)

L. H. Smedsrud, Bjerknes Center for Climate Research, Allegaten 57, N-5007 Bergen, Norway.